www.sciencemag.org/content/343/6175/1140/suppl/DC1

Supplementary Materials for

Mechanism of the C5 Stereoinversion Reaction in the Biosynthesis of Carbapenem Antibiotics

Wei-chen Chang,* Yisong Guo, Chen Wang, Susan E. Butch, Amy C. Rosenzweig, Amie K. Boal,* Carsten Krebs,* J. Martin Bollinger Jr.*

*Corresponding author. E-mail: oscarntu@gmail.com (W.-c.C.); akb20@psu.edu (A.K.B.); ckrebs@psu.edu (C.K.); jmb21@psu.edu (J.M.B.)

Published 7 March 2014, *Science* **343**, 1140 (2014)
DOI: 10.1126/science.1248000

This PDF file includes:

Materials and Methods
Figs. S1 to S15
Table S1
References

Science
AAAS

Supplementary Materials for

Mechanism of the C5 Stereoinversion Reaction in the Biosynthesis of Carbapenem Antibiotics

Correspondence to oscarntu@gmail.com; akb20@psu.edu; ckrebs@psu.edu; jmb21@psu.edu

Wei-chen Chang, Yisong Guo, Chen Wang, Susan E. Butch, Amy C. Rosenzweig, Amie K. Boal, Carsten Krebs, and J. Martin Bollinger, Jr.

Materials and Methods

Materials. NMR spectra were recorded on a Bruker 300, 360 or 400 MHz spectrometer at the Nuclear Magnetic Resonance Facility of the Chemistry Department, The Pennsylvania State University. Chemical shifts (δ in ppm) are given relative to that of solvent ($CDCl_3$, MeOD or D_2O), with coupling constants reported in Hertz (Hz). Analytical thin-layer chromatography (TLC) was carried out on pre-coated TLC aluminum plates (silica gel, grade 60, F_{254}, 0.25 mm layer thickness) acquired from EMD Chemicals (Gibbstown, NJ). Flash-column chromatography was performed using silica gel (230-400 mesh, grade 60) obtained from Sorbent Technologies. Liquid chromatography/mass spectrometry (LC-MS) analyses were carried out on an Agilent 1200 series LC system connected to a triple-quadrupole mass spectrometer, Agilent 6400 (Agilent Technologies). $Fe(NH_4)_2(SO_4)_2$ was purchased from J. T. Baker (Philipsburg, NJ). ^{57}Fe metal was purchased from Advanced Materials and Technology, Incorporated (New York, NY). All reagents were used directly as obtained from the commercial sources.

DNA Construct for Over-expression of Carbapenem Synthase (CarC). The DNA sequence encoding carbapenem synthase (CarC) from *Pectobacterium carotovorum* was codon-optimized for over-expression in *E. coli*, synthesized, and inserted into the *Nde*I and *BamH*I restriction sites of expression vector pET-28a by GeneArt (Regensburg, Germany). This plasmid construct, which places the gene under the control of a T7 promoter, allows for overproduction of the protein containing an *N*-terminal hexa-histidine tag. The final construct was verified by DNA sequencing at the Molecular Core Facility of The Pennsylvania State University. The codon-optimized gene sequence is shown below.

ATGAGCGAGATCGTGAAATTTAACCCGGTTATGGCAAGCGGTTTTGGT
GCATATATTGATCATCGTGATTTTCTGGAAGCCAAAACCGAAACCATTAAAA
ACCTGCTGATGCGTCAGGGTTTTGTGGTTGTTAAAAACCTGGATATTGATAGC
GATACCTTCCGCGATATCTATAGCGCCTATGGCACCATTGTTGAATATGCCGA

TGAAAAAATTGGTGTGGGTTTTGGTTATCGCGATACCCTGAAACTGGAAGGT
GAAAAAGGTAAAATTGTTACCGGTCGTGGTCAGCTGCCGTTTCATGCAGATG
GTGGTCTGCTGCTGAGCCAGGTTGATCAGGTTTTTCTGTATGCAGCCGAAATC
AAAAACGTGAAATTTCGTGGTGCAACCACCGTTTGTGATCATGCACTGGCAT
GTCAAGAAATGCCTGCACATCTGCTGCGTGTTCTGGAAGAAGAAACCTTTGA
AGTTCGTGTGCTGGAACGTGGTTATTATGTTGATGTTAGTCCGGATGGTTGGT
TTAAAGTTCCGGTTTTTACCGATCTGGGTTGGGTTCGCAAAATGCTGATCTAT
TTTCCGTTTGATGAAGGTCAGCCTGCAAGCTGGGAACCGCGTATTGTTGGTTT
TACCGATCATGAAACCCAGGCCTTTTTTCAAGAACTGGGTGCATTTCTGAAAC
AGCCTCGCTATTATTACAAACACTTTTGGGAAGATGGCGACCTGCTGATTATG
GATAATCGTCGTGTTATTCATGAACGCGAAGAGTTCAACGATGATGATATTGT
TCGTCGTCTGTATCGTGGTCAGACCGCAGATATTTAAGGATCC

DNA Constructs for Over-expression of Tyr→Phe CarC Variants. Tyr→Phe (Y→F) substitutions at Y67, Y164, Y165 and Y191 were generated using the primers in the following table and the Stratagene QuikChange II kit according to the manufacturers instructions:

Primer name		sequence
CarC-Y67F	Forward	5'-GCCTATGGCACCATTGTTGAA**TTT**GCCGATGAAAAAATTGGT-3'
	Reverse	5'-ACCAATTTTTTCATCGGC**AAA**TTCAACAATGGTGCCATAGGC-3'
CarC-Y164F	Forward	5'-CGTGTGCTGGAACGTGGT**TTT**TATGTTGATGTTAGTCCG-3'
	Reverse	5'-CGGACTAACATCAACATA**AAA**ACCACGTTCCAGCACACG-3'
CarC-Y165F	Forward	5'-GTGCTGGAACGTGGTTAT**TTT**GTTGATGTTAGTCCGG -3'
	Reverse	5'-CCGGACTAACATCAAC**AAA**ATAACCACGTTCCAGCAC -3'
CarC-Y191F	Forward	5'-CGCAAAATGCTGATC**TTT**TTTCCGTTTGATGAAGG -3'
	Reverse	5'-CCTTCATCAAACGGAAA**AAA**GATCAGCATTTTGCG -3'

Over-expression and Purification of CarC and Tyr→Phe Variants. Plasmid encoding wild-type (wt) or variant CarC genes were used to transform *E. coli* BL21(DE3) (Invitrogen; Carlsbad, CA) for protein production. A single colony was used to inoculate a starter culture, which was incubated overnight at 37 °C. Production cultures were grown at 37 °C in Luria–Bertani (LB) medium supplemented with 50 μg/mL kanamycin to OD_{600nm} ~ 0.6 and then cooled to 18 ^{o}C. The expression of CarC gene was then induced by addition of IPTG to a final concentration of 1.0 mM. The cultures were grown for 16 h at 18 °C before they were harvested by centrifugation.

Purification was performed at 4 ºC. In a typical purification, ~60 g wet cell paste was re-suspended in 180 mL lysis buffer (100 mM Tris•HCl and 5 mM imidazole, pH 7.5) with addition of PMSF to a final concentration of 1.0 mM. The cells were subjected to four 8 min bursts of the (Microfluidics, M110EH-30, Newton, MA) microfluidizer operating at ~20 kpsi. The cell lysate was then centrifuged at 22,000 x *g* for 30 min at 4 °C to remove cellular debris. The supernatant was then loaded onto the Ni-NTA column (1:3=volume column:volume of clarified lysate). After loading, the column was washed with 400 mL of lysis buffer (100 mM Tris•HCL, 5.0 mM imidazole, pH 7.5) before the

protein was eluted by washing with 100 mM Tris•HCl, 250 mM imidazole, pH 7.5 (elution buffer). Fractions containing the protein were pooled and concentrated in a centrifugal concentrator with 10 kDa molecular weight cut-off (Pall Corporation, Port Washington, NY). The concentrated protein was exchanged into CarC reaction buffer (100 mM Tris•HCl, pH 7.5) by dialysis overnight. Protein concentration was determined by UV absorption at 280 nm using a calculated molar absorptivity of 41,370 $M^{-1}cm^{-1}$ (http://ca.expasy.org). From 60 g of wet cell paste, ~1.2 g of protein was obtained. The purity of the protein was shown by SDS–PAGE (12%) (fig. S1).

Synthetic Methods. (3*S*,5*S)*-carbapenam, **3**, its 5-deuterium-substituted isotopologue ((3*S*,5*S*)-[5-^{2}H]-carbapenam; 5-*d*-**3**), and (3*S*,5*R)*-carbapenam, **4**, were synthesized by variants of published procedures, as summarized in fig. S2 and described in the text below.

Following the published procedure (*45*), a solution of $LiBEt_3H$ (1M in THF, 24 mL, 24 mmol) was added slowly to (*S*)-1-*t*-butyl-2-methyl 5-oxopyrrolidine-1,2-dicarboxylate (5.1 g, 20 mmol, dissolved in 20 mL THF) at -78 ^oC using an addition funnel. After this addition, the reaction was stirred at the same temperature for 30 min with monitoring by TLC. The reaction was quenched by addition of 20 mL saturated aqueous $NaHCO_3$ solution, and a few drops of H_2O_2 solution (30% w/v) were then added at 0 ^oC. The organic layer was extracted using CH_2Cl_2 (3 x 20 mL). The combined organic (CH_2Cl_2) layer was dried over $MgSO_4$, and the solvent was removed *in vacuo*. The crude product was used in the next step without further purification. The deuterium-containing isotopolog was prepared simply by replacing $LiBEt_3H$ with $LiBEt_3{}^2H$ to incorporate deuterium at this step.

Following the published procedure (*46*), *t*-butyl-2-(diethoxyphosphoryl)acetate (5.0 g, 19.8 mmol) was added at room temperature to a solution of NaH (60% with mineral oil, 793 mg, 19.8 mmol) in DMF (50 mL), and the reaction was stirred for 1 h. Compound **5** (4.05 g, 16.8 mmol) dissolved in 50 mL DMF was then added at the same temperature, and the reaction was incubated for ~12 h. The reaction was quenched by addition of an aqueous saturated NH_4Cl solution (100 mL) and extracted with Et_2O (3 × 50 mL). The combined organic layer was washed with brine (50 mL), dried over $MgSO_4$, and concentrated under reduced pressure. The crude product was purified by flash chromatography on silica gel with hexanes/ethyl acetate (3:1) as the eluent to give (2*S*,5*S*)-1-*t*-butyl-2-methyl-5-(2-(*t*-butoxy)-2-oxoethyl)-pyrrolidine-1,2-dicarboxylate, **6**, in 65% yield over the two steps.

The *t*-butyl ester of **6** was hydrolyzed by addition of trifluoroacetic acid (TFA, 2.0 mL) at room temperature to a solution of **6** (690 mg, 2.0 mmol) in CH_2Cl_2 (6.0 mL). The reaction was allowed to proceed to completion (as determined by TLC) over ~ 10 h, yielding methyl ester **6'**. The crude reaction was first concentrated under reduced pressure and then subjected to full vacuum to remove the residual TFA. The product (**6'**, a light yellow oil) was used directly without further purification.

Cyclization of **6'** to form β-lactam, **7**, was carried out by using the Mukaiyama reagent according to the published procedure (*47*). A solution of 2-chloro-1-

methylpyridinium iodide (2.04 g, 8.0 mmol) in acetonitrile (100 mL) was treated with triethylamine (2.33 mL, 16.8 mmol) at room temperature, and the reaction was then incubated at 70 ^{o}C for 30 min. The crude **6'** from the previous reaction was dissolved in approximately equal volume of acetonitrile and cannulated into the reaction at the same temperature, and the reaction mixture was cooled gradually to room temperature and stirred for an additional 48 h. The reaction was evaporated, dissolved in ethyl acetate (100 mL) and washed with water (4 x 30 mL). The organic layer was concentrated under reduced pressure, and the crude reaction mixture was purified by flash chromatography on silica gel with 1:1 hexanes/ethyl acetate as eluent to afford methyl-(3*S*,5*S*)-carbapenam-3-carboxylate, **7**, in 15% yield. The ^{1}H-NMR spectrum of **7** (fig. S2B, bottom trace) was consistent with the previously published spectrum (*35*, *48*).

According to a published procedure (*33*, *48*), enzymatic hydrolysis of methyl ester **7** using porcine liver esterase (Sigma-Aldrich, St. Louis, MO) was carried out with 0.01 mmol **7** per mg esterase. The reaction was monitored by ^{1}H-NMR (*Figure S1*), which showed that ester hydrolysis reached completion in 30 min, affording final product (3*S*,5*S*)-carbapenam, **3**; ES-MS calculated for $C_7H_9NO_3$ *m*/*z* 155.15, found ($M–H^+$) *m*/*z* 154.00. After the reaction, the esterase was removed by passing the solution through a Nanosep centrifugal filter (Pall Corporation, Port Washington, NY), and the resulting filtrate was used directly in the CarC reactions.

To obtain a standard for (3*S*,5*R*)-carbapenam, **4**, an alternative approach, adapted from a published procedure (*33*), was taken. A solution of *t*-butyl acetate (2.19 g, 18.9 mmol dissolved in 20 mL of THF) was dripped into 50 mL of a solution of lithium diisopropylamide (2.0 M, 8.6 mL, 17.3 mmol in THF kept cold in a dry ice/acetone bath. After the reaction was stirred at the same temperature for 30 min, (*S*)-1-benzyl 2-methyl-5-oxopyrrolidine-1,2-dicarboxylate, **8** (4.0 g, 14.5 mmol, dissolved in 20 mL THF) was added slowly. The reaction was stirred for an additional 1 h. The reaction was quenched by addition of an aqueous saturated NH_4Cl solution (100 mL) and extracted with ethyl acetate (2 x 50 mL). The combined organic layer was evaporated under reduced pressure, and the crude product was purified by flash chromatography on silica gel with 2:1 hexanes/ethyl acetate as mobile phase, affording product **9** in 34% yield.

The deprotection of **9** followed by *in situ* cyclization and reductive amination favored formation of *cis* product **10** over its *trans* diastereomer. A few drops of concentrated acetic acid was added to a solution of **9** (2.65 g, 6.73 mmol) in methanol (30 mL), and the reaction mixture was subjected to hydrogenolysis and hydrogenation using a catalytic amount of palladium carbon (10%, ~ 40 mg) at atmospheric pressure for 48 h. The catalyst was removed by filtration, and the filtrate was concentrated. The crude reaction mixture was purified by silica gel chromatography with 2:1 hexanes/ethyl acetate containing 3% methanol as mobile phase, yielding a mixture of **10** and its *trans* diastereomer with a precise ratio of 1.8:1 (as determined by ^{1}H-NMR) and an overall yield of 33%.

Analogously to the two-step procedure used to convert **6** to methyl-(3*S*,5*S*)-carbapenam-3-carboxylate, **7**, the mixture of **10** and its *trans* diastereomer was treated with TFA to give **10'** and **6'**, and this product was subjected to cyclization using the

Mukaiyama reagent. Purification by flash column chromatography afforded a 3.5:1 mixture of methyl-(3*S*,5*R*)-carbapenem-3-carboxylate, **11**, and **7** in an overall yield of 16.7%. The ^{1}H NMR spectrum of **11** is consistent with the previously published spectrum (*35*). Hydrolysis of the methyl ester by porcine liver esterase, as described above, yielded the 3.5:1 mixture of **4:3** that was used as the standard for **4** in the LC-MS analysis of Fig. 4D and fig. S8.

When treated with formic acid quench solution in the chemical-quenched-flow experiment (Fig. 4D), the β-lactam ring of **3** or **4** is hydrolyzed to afford the corresponding product, *trans*-5-carboxymethyl-L-proline, **12**, or *cis*-5-carboxymethyl-L-proline, **13** (fig. S14A). Standards enriched in either **12** or **13** (fig. S14B) were also obtained from precursors enriched in either **10'** or **6'** by the synthetic methods. Esterase-catalyzed hydrolysis of the methyl esters, as described above, converted **6'** and **10'** to **12** and **13**, respectively. The synthetic *trans* compound, **12**, was obtained in nearly pure form, but the synthetic *cis* diastereomer, **13**, was obtained only as a 1.8:1 mixture of **13**:**12**, owing to the limited stereoselectivity in the cyclization of **9**.

Transient Kinetics Experiments. General procedures for the stopped-flow absorption and freeze-quench experiments have been published (*31*, *41*). Stopped-flow experiments were carried out on an Applied Photophysics SX-200 stopped-flow spectrometer (Leatherhead, UK). An O_2-saturated buffer solution (100 mM Tris•HCl, pH 7.5) was mixed with an equal volume of an O_2-free solution containing CarC (1.0 mM), Fe(II) (0.8 mM), 2OG (20 mM) and substrate **3** (10 mM). The experiments monitored the kinetics of the tyrosyl radical (Y•) intermediate by its absorbance at 410 nm. To resolve the kinetics of the Y• from absorbance changes contributed by other species, the thoroughly validated $A_{410\ \mathrm{dropline}}$ approach was used, as illustrated in Fig. 4A (*49*). Non-linear regression analysis of kinetic traces was carried out with the program Kaleidagraph (Synergy Software, Reading, PA). Details of the analysis are provided in the caption to fig. S7.

Freeze-quench experiments were carried out by using an Update Instruments (Madison, WI) model 1000 freeze-quench/chemical-quench apparatus. Analogously to the stopped-flow experiments, an O_2-saturated buffer solution (100 mM Tris•HCl, pH 7.5) was mixed with an equal volume of an O_2-free solution containing CarC, Fe(II), 2OG and substrate **3**. For anaerobic control samples, the O_2-free solution was mixed with an equal volume of O_2-free buffer and the mixture was frozen under anoxic conditions. For the Mössbauer and EPR samples, the concentrations after mixing were 1.1 mM CarC, 0.88 mM ^{57}Fe(II), 10 mM 2OG, 5.0 mM substrate **3**, and ~ 0.9 mM O_2.

The chemical-quenched-flow experiment (Fig. 4D) was performed similarly to the freeze-quench experiment by using the Update Instruments apparatus. The concentrations of the reactants after mixing were 0.78 mM CarC, 0.625 mM Fe(II), 1.0 mM 2OG, 0.125 mM **3**, and ~ 0.9 mM O_2. [2,2,3,3-$^{2}H_4$]-succinate (d_4-succinate) was present in the protein reactant syringe at 0.50 mM as an internal standard for quantification of the succinate co-product (fig. S8A,B). The reaction was terminated by injecting the reaction solution into a microcentrifuge tube containing four equivalent volumes of 90% isopropanol/10% formic acid (v/v). Prior to LC-MS analysis, samples were filtered through Nanosep

centrifugal filters (Pall Corporation, Port Washington, NY) to remove protein, and dried in a SpeedVac concentrator (Thermo Scientific, Bellefonte, PA). The samples were re-dissolved in 0.2 mL of water and then subjected to LC-MS analysis.

LC-MS Analysis of the CarC Reaction Products. High performance liquid chromatography (HPLC) with detection by mass spectrometry (LC-MS) was conducted on an Agilent Technologies (Santa Clara, CA) 1200 system coupled to an Agilent Technologies 6410 QQQ mass spectrometer. The associated Agilent MassHunter software package was used for data collection and analysis. Assay mixtures (5 μL) were separated on an Agilent Technologies Poroshell 120 HILIC column (4.6 x 50 mm, 2.7 μm particle size) equilibrated in 5% solvent A (95:5 v/v H_2O:CH_3CN) and 95% solvent B (5:95 v/v H_2O:CH_3CN). Both solvents were supplemented with 0.1 % formic acid. The elution program was: 95% to 80% B from 3 to 5 min; 80% to 60% B from 5 to 12 min; 60% to 35% B from 12 to 14 min; and 35% to 95% B from 14 to 16 min with the flow rate of 0.4 mL min^{-1}. The column was allowed to re-equilibrate for 4 min at 95% B before the next sample injection. Detection of products was achieved by electrospray ionization in negative mode (ESI^-).

In generating the red and blue traces in Fig. 4D and fig. S14B labeled shorthand as **3**→**12** and **4**→**13**, respectively, the >98% pure synthetic standard for **3** and the 3.5:1 **4**:**3** standard synthesized as described above were treated with formic acid to give >98% pure **12** and a 3.5:1 mixture of **13**:**12**, respectively, which were subjected to the LC-MS analysis. The presence of **12** in the sample from hydrolysis of the 3.5:1 **4**:**3** standard is evidenced by the minor peak at 7.8 min elution time in the blue trace. The central traces in fig. S14B (*purple and green*) are from injection of samples of the nearly pure **12** and the 1.8:1 **13**:**12** standards obtained via esterase treatment of **6'** and 1.8:1 **10'**:**6'**, respectively, as described above.

EPR and Mössbauer Spectroscopy. Mössbauer spectra were collected on two spectrometers. The spectrometer used to acquire the weak-field (53 mT) spectra is equipped with a Janis SVT-400 variable-temperature cryostat, whereas the spectrometer used to acquire the strong-field (8.0 T) spectra is equipped with a Janis 8T MOSS-OM-12SVT variable-temperature cryostat. The external magnetic field was applied parallel to the γ-beam. Isomer shifts are quoted relative to Fe metal at 298 K. Mössbauer spectral simulations were performed using WMOSS software package (See Co., Edina, MN). EPR spectra were recorded on two spectrometers: a Bruker ESR 300 spectrometer equipped with ER 041 MR microwave bridge, and a Bruker E580 spectrometer equipped with SuperX FT microwave bridge. Each spectrometer is equipped with an Oxford ESR 900 liquid helium cryostat and an Oxford temperature controller ITC 503S. Spin quantifications of EPR signals were performed by comparison to the signal from a Cu^{II} spin standard with concentration of 1.025 mM measured under non-saturating conditions. A packing factor of 0.55 was used for all the spin quantifications on EPR spectra of freeze-quenched samples.

Spectral Simulations. Simulations of the X-band EPR spectra were carried out by using the program SpinCount developed by Prof. Michael P. Hendrich in the Department

of Chemistry at Carnegie Mellon University. For simulations of the spectrum of the Y• at 100 K, the spin-Hamiltonian in Eq 1 was used (S_{tyr} = 1/2):

$$\mathcal{H} = \beta \mathbf{S}_{\mathbf{tyr}} \cdot \mathbf{g} \cdot \mathbf{B} + \sum_{i=1,4} \mathbf{S}_{\mathbf{tyr}} \cdot \mathbf{A}_{(\mathrm{H})i} \cdot \mathbf{I}_{(\mathrm{H})i} \qquad (1)$$

The first term in Eq 1 describes the electron Zeeman interaction, the second term describes the electron-nuclear hyperfine interactions between the electron spin on the Y• and 4 hydrogen nuclei ($H_{\beta 1,2}$ and $H_{3,5}$). For Mössbauer simulations, the spin-Hamiltonian in Eq 2 was used:

$$\mathcal{H} = D\left[\mathbf{S}_z^2 - \frac{S(S+1)}{3} + \frac{E}{D}\left(\mathbf{S}_x^2 - \mathbf{S}_y^2\right)\right] + \beta \mathbf{S} \cdot \mathbf{g} \cdot \mathbf{B} + \mathbf{S} \cdot \mathbf{A}_{57Fe} \cdot \mathbf{I}_{57Fe} + \frac{eQV_{zz}}{12}\left[3\mathbf{I}_z^2 - \frac{15}{4} + \eta\left(\mathbf{I}_x^2 - \mathbf{I}_y^2\right)\right] - g_n \beta_n \mathbf{B} \cdot \mathbf{I}_{57Fe} \qquad (2)$$

The first term in Eq 2 describes the axial and rhombic zero-field splitting, the second term is the electron Zeeman interaction, the third term is the electron-nuclear hyperfine interactions between the electron spin and ^{57}Fe nucleus, the fourth term is the ^{57}Fe quadruple interaction, and the last term is the ^{57}Fe nuclear Zeeman interaction.

*X-ray Crystal Structure of the CarC•Fe(II)•2OG•**3** Complex.* *P. carotovorum* CarC apoprotein (20 mg/mL in 50 mM Tris-HCl) was rendered anoxic on a vacuum line by 5 cycles of evacuation and Ar purge). One equivalent $(NH_4)_2Fe(SO_4)_2$ and 5 equivalents 2OG were added to the protein in a Coy anaerobic chamber. To prevent reaction of the Fe(II) center with O_2, all subsequent manipulations were carried out anaerobically with stringently deoxygenated solutions. The CarC sample was crystallized at room temperature using the hanging-drop vapor diffusion method with 0.1 M HEPES, pH 7.0, 15% (v/v) isopropanol, and 0.2 M ammonium acetate as the precipitating solution. To incorporate substrate, drops with crystals were overlaid with a solution of freshly prepared substrate **3** (degassed and diluted in well solution to a final concentration of 2.5 mM) and allowed to soak for two hours at room temperature in the anaerobic chamber. Crystals were mounted on rayon loops and flash-frozen in liquid nitrogen for data collection following a brief additional soak in well solution supplemented with 25% (v/v) glycerol as cryoprotectant.

Crystallographic datasets were collected at the Life Sciences Collaborative Access Team beamlines at the Advanced Photon Source and processed using the HKL2000 software package (*50*). The structure was solved by molecular replacement using PHASER (*51*) with the *P. carotovorum* CarC crystal structure (PDB accession code 1NX4) as the initial search model. Refinement and model building were performed with Refmac5 (*52*) and Coot (*53*). Coordinates and geometric restraints for substrate **3** were generated with the PRODRG2 server (*54*). Table S1 reports all data collection and refinement statistics.

The asymmetric unit (ASU) consists of three CarC monomers, designated chains A-C, with a hexameric quaternary structure related by crystallographic symmetry, as reported in previous structural studies on the enzyme (*36*). Secondary structure matching (SSM) superposition (*55*) of the three monomers in the ASU shows an identical overall fold (0.5 Å rmsd for 241 Cα atoms) for all three subunits. Notable exceptions involve three localized regions of the sequence. They include three loops, comprising residues 67-78 (*loop 1*), 104-109, and 161-171 (*loop 2*). Loop 1 is partially disordered in chain A,

and several ordered residues occupy different positions than in chains B and C. Residues 104-109 are ordered in chain A but also occupy different positions than in the other two chains. These loops normally (in chains B and C, which most likely represent the active conformation) fold over the active site but are distorted in chain A due to a crystallization contact between symmetry-related monomers (fig. S5). Loop 2 (161-171) near the active site also remains disordered in chain A. The lattice contact and consequent distortion of the active site and "lid" loops seem to prohibit facile binding of **3** in chain A. Weak electron density for the substrate is present in this chain (fig. S4), suggesting partial occupancy, but the orientation of the molecule cannot be unequivocally determined from the electron density map. Therefore, only residues 2-67, 74-160, and 172-272 can be modeled in monomer A, consistent with observations on the crystal structures of CarC lacking a ligand (PDB accession code 1NX4) or having *N*-acetyl-L-proline bound at the substrate site (PDB accession code 1NX8). In monomers B and C, however, a continuous chain can be traced from 2-272, strong electron density from the substrate is seen in both active sites, and the orientation of the substrate can be unambiguously determined from this electron density (fig. S4). The final model includes residues 2-272 in chain B; residues 2-272 in chain C; residues 2-67, 74-160, and 172-272 in chain A; three Fe(II) ions; three 2OG molecules; two substrate (**3**) molecules; one glycerol molecule; and 611 water molecules. Ramachandran plots generated with PROCHECK (*56*) and Molprobity (*57*) place 99.7% of residues in allowed and generously allowed regions. Figures were generated with the PyMOL Molecular Graphics System (Schrödinger, LLC) and electron-density maps were calculated with FFT (*58*).

Supplementary Figures and Table

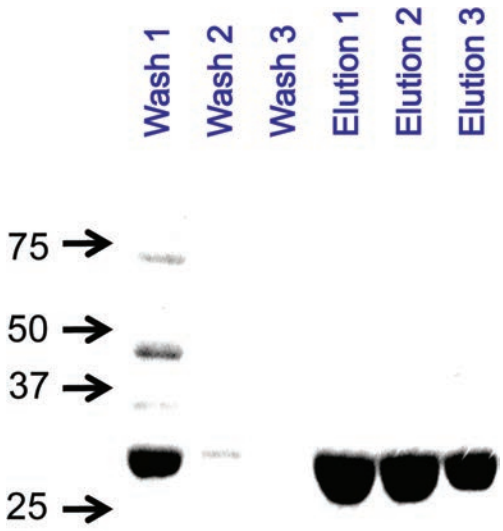

Figure S1. Coomassie-stained 12% SDS-PAGE analysis of *N*-terminally hexa-histidine-tagged CarC. The arrows indicate the positions of molecular weight standards; lanes 1-3 are wash fractions from the metal-ion-affinity chromatography; lanes 4-6 are the elution fractions from the purification.

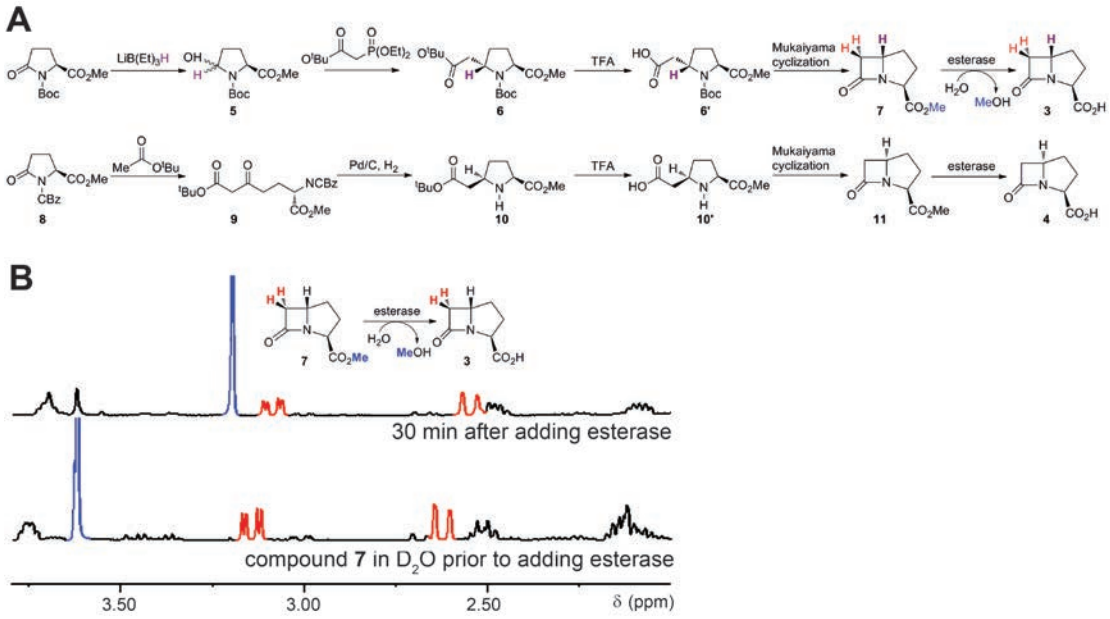

Figure S2. (***A***) Synthetic schemes used to prepare carbapenams **3** and **4**, and (***B***) ^{1}H-NMR spectra monitoring hydrolysis of the methyl ester **7** (to yield **3**) catalyzed by porcine liver esterase.

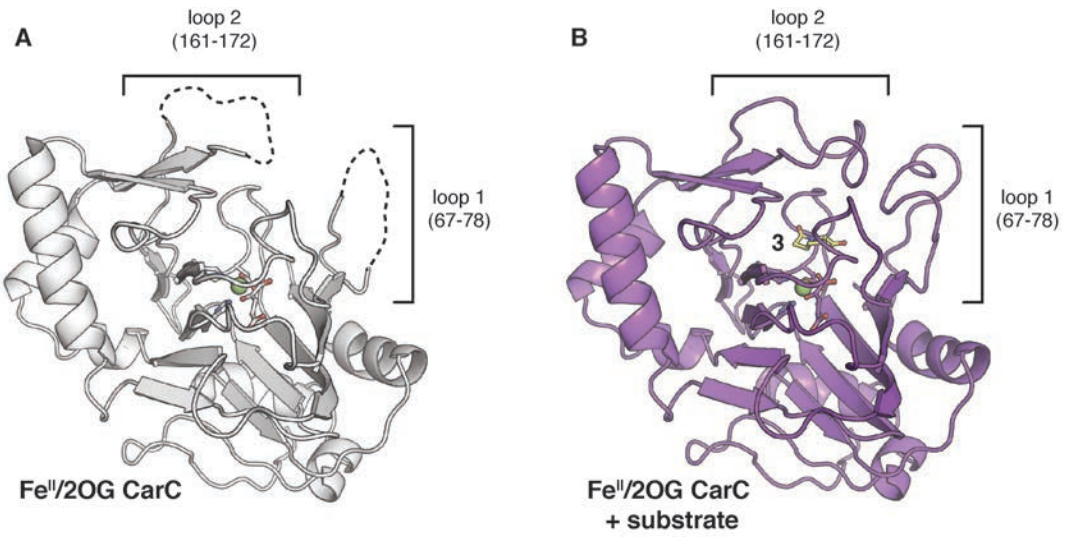

Figure S3. Ribbon diagram comparing the overall structure of CarC in the absence (***A***) (PDB accession code 1NX4) and presence (***B***) of carbapenam **3** (***yellow ball and stick format***). The Fe(II) cofactor and 2OG co-substrate are shown as ***green spheres*** and ***white or purple sticks***, respectively. Disordered loops in the structure of CarC•Fe(II)•2OG (lacking **3**) are indicated by ***dashed black lines***.

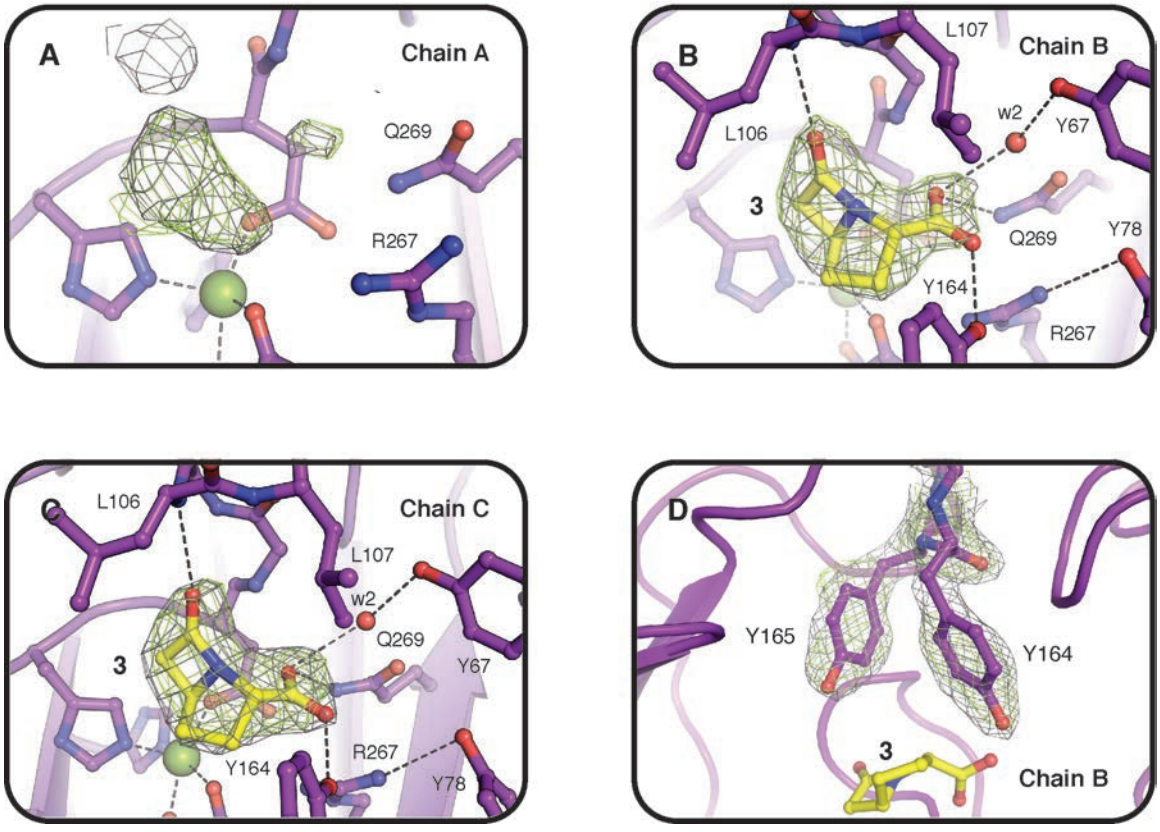

Figure S4. Electron density maps associated with **3** in each CarC chain in the ASU. The ***gray mesh*** shows the $2F_o$-F_c map contoured at 1.2σ. The ***green mesh*** shows the F_o-F_c omit map, contoured at 2.6σ. Panels ***A***-***C*** show chains A-C, respectively. While significant electron density is present for **3** in chains B (***B***) and C (***C***), with clearly identifiable carbonyl and carboxylate substituents, chain A (***A***) exhibits only weak electron density in the active site. The observation of at least some density in chain A suggests either that **3** may be bound in only a fraction of the chain A molecules or that it is partially disordered or bound in multiple orientations. Because the active site is also distorted in this monomer due to a crystallization contact (*fig. S5*), the substrate was not modeled into chain A. (***D***) Electron density maps (color coded as in ***A***-***C***) for Y164 and Y165 in newly resolved loop 2 (*fig. S3*).

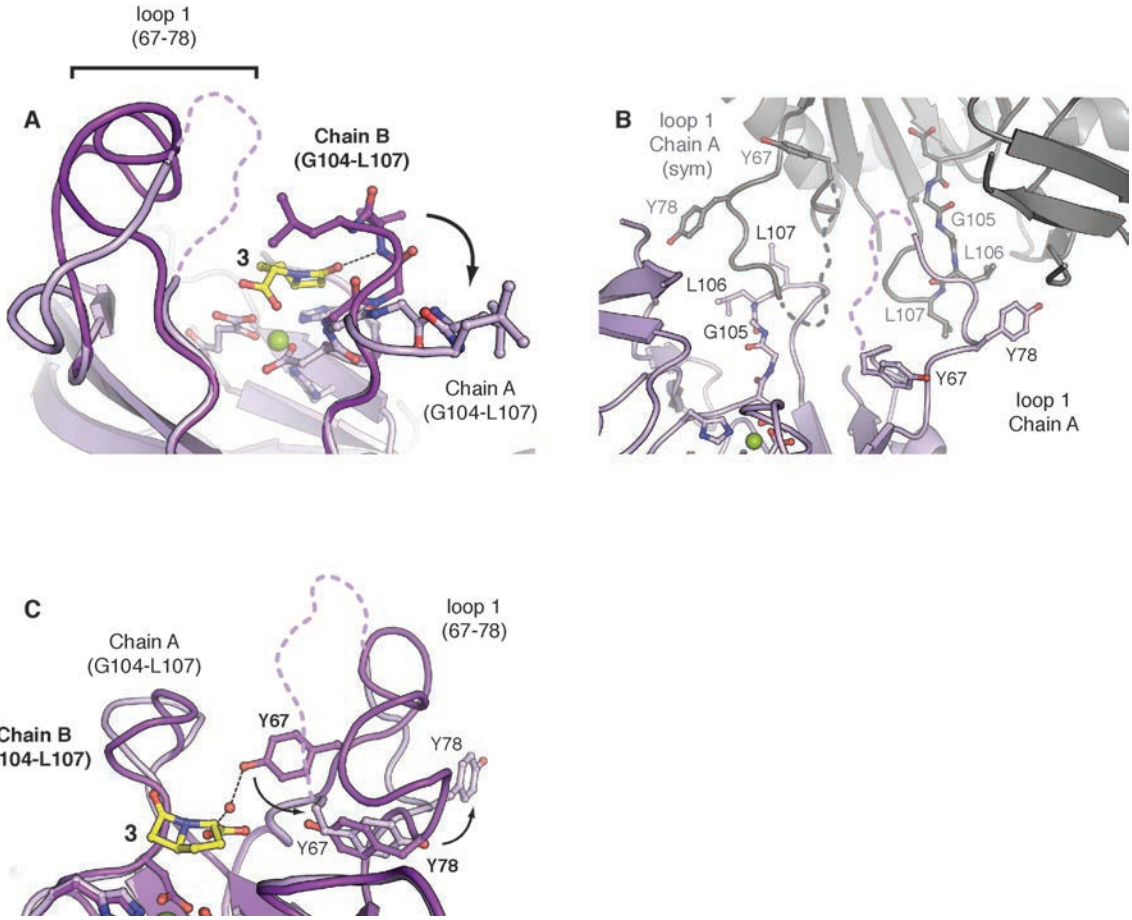

Figure S5. Remodeling of loops associated with a crystal lattice artifact in chain A. (***A***) Comparison of chains A (***lighter pink***) and B (***purple***) to illustrate the remodeling of a short active-site loop (***residues 104-107***) and longer "lid" loop 1 (***residues 67-78***) associated with crystal lattice artifact. (***B***) The short loop in chain A is distorted by invasion of loop 1 from another chain A molecule related by crystallographic symmetry (***gray***). Note that this monomer is not the chain A symmetry mate that forms the hexamer. The inter-chain invasion of loop 1 results in a severe bending of the short loop (***104-107***)

in the invaded monomer away from the substrate-binding site, which increases the solvent exposure and is probably a critical feature of the failure of chain A to properly order the substrate. Note that residues 104-107 are required to form a key hydrogen-bonding contact with the carbonyl substituent of **3** (*Fig. 2A*). (***C***) The crystallization artifact alters the locations of two loop 1 Y residues (***Y67, Y78***) near the active site. In chains B and C, with well-ordered substrate, Y67 is part of a water-mediated hydrogen-bonding network involving the carboxylate substituent of substrate **3** (***ball-and-stick format with yellow carbon atoms***). Y78 sits at the base of loop 1, supporting the secondary structure of the loop and participating in another hydrogen-bonding network involving **3**. Both residues additionally appear to be critical for blocking bulk solvent access to the active site. In chain A, Y78 adopts a new position that is entirely driven by its involvement in the lattice contact and almost certainly artificial. Y67 then approaches from the opposite direction to fill the spot vacated by Y78. In contrast to the scenario for Y78, the chain A conformation for Y67 may represent its true position in the absence of substrate, because it is found in this location in two of the three monomers in the previously reported X-ray crystal structures of CarC having no ligand bound (PDB accession code 1NX4) or *N*-acetyl-L-proline bound (PDB accession code 1NX8) at the substrate site (*36*). Thus, displacement of Y67 by Y78 could be an authentic component of the substrate-driven ordering transition observed in the structure of loop 1. The lattice artifact in chain A is also present in the chain B monomers of the previously published structures, and the structure of this monomer was subsequently used as the basis for computational modeling studies to analyze the mechanism (*28*). In this computational study, the deduced position of the substrate is similar to that observed here and was cited as being consistent with the proposal of H• abstraction from C5 of **3** by the ferryl intermediate. However, the modeling work pinpointed Y67 as the most likely candidate to be the H• donor in the subsequent step of the stereoinversion reaction (*28*). In the published study, the mechanistic conclusions relied solely on the previously published crystallographic models of the CarC monomer containing the above-described artifact and lacking complete structural information for loops 1 and 2. Consequently, it concluded that the active site is much more open and accessible than it actually is in the CarC•Fe(II)•2OG•**3** structure. The side chain of Y67 therefore appears able to swing into position to donate the H• to the C5 position to produce **4**. The new CarC•Fe(II)•2OG•**3** structure reveals that such conformational changes would be prohibited by the new position of Y78 and by interaction of Y67 with the carboxylate substituent of **3**. Instead, Y67 probably functions primarily in substrate binding and in limiting solvent accessibility in the active site during the reaction. Y67, together with Y78, may also be an important driver of the loop 1 reorganization that is necessary for the binding and release of substrate and product. Finally, Y67 and Y78, together with four additional aromatic residues arrayed in the substrate binding pocket within 10 Å of **3**, could potentially have a role in delocalization and stabilization of the protein radical equivalent initially formed on Y165. Any of these functions would be consistent with the perturbed Y• kinetics in the Y67F, Y164F, and Y191F variant proteins (*Fig. 4B*).

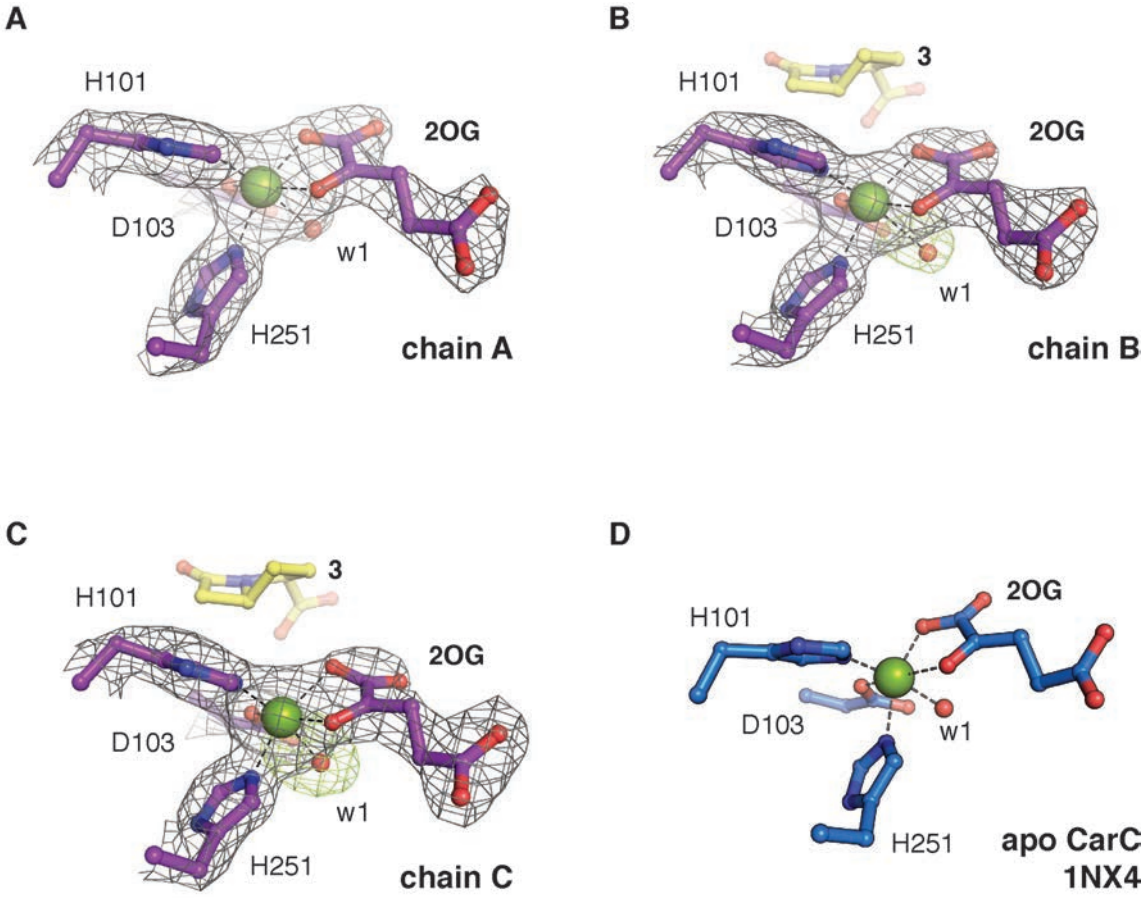

Figure S6. Electron density maps comparing active-site structures in chain A (lacking bound substrate) and chains B and C with **3** bound. (***A***-***C***) Chains A-C. $2F_o$-F_c electron density maps contoured at 1.2σ are shown as ***gray mesh***, and omit maps contoured at 3.0σ are shown as ***green mesh***. (***D***) Active site configuration in the published structure with no ligand in the substrate site (PDB accession code 1NX4). In the absence of substrate **3**, a water molecule occupies the presumptive O_2 addition site in a location distal to the substrate-binding site, and it has been proposed previously that the Fe(II) coordination geometry must change prior to the reaction (*21*). Because the active site configuration in the CarC•Fe(II)•2OG•**3** structure is nearly identical to that in the absence of **3**, it does not appear that substrate binding is the trigger for the proposed change in cofactor coordination. A comparison of the electron density maps for the active sites in monomers B (***B***) and C (***C***) to those in A (***A***) reveals a subtle increase in the lability of the coordinated water molecule that may be an important preface to O_2 binding and the requisite coordination change. In chain A, significant $2F_o$-F_c electron density is present for the water ligand after its inclusion in the model and subsequent refinement. In chains B and C, with **3** bound at full occupancy, a water molecule has also been added to the active site model to satisfy positive F_o-F_c difference density present (green mesh) prior to refinement but little $2F_o$-F_c density emerges afterwards. Additionally, the temperature factors for the coordinated water are higher in chains B and C (B = 55-65) than in chain A (B = 45), suggesting a distinct decrease in the occupancy or increase in the disorder of the labile water ligand in the monomers containing **3**. These structural changes are

perhaps also consistent with the observation of "substrate-triggering" of O_2 addition in CarC (*Fig. 4B, red and orange traces*).

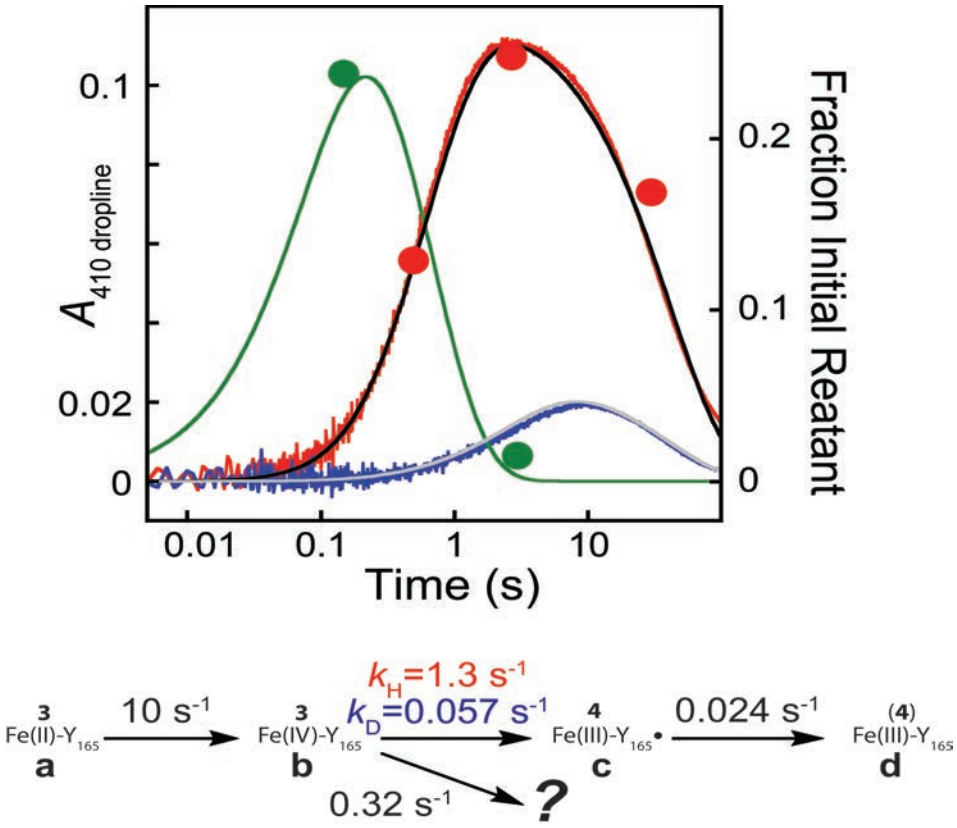

Figure S7. Kinetic analysis of the reaction of the CarC•Fe(II)•2OG•**3**/5-*d*-**3** complex with excess O_2 at 5 °C. The ***red and blue traces***, which are associated with the left-hand y-axis, are A_{410}-(A_{404}+A_{416})/2 ($A_{410\ dropline}$, proportional to the concentration of Y•) from the average of three stopped-flow trials each for the reaction with **3** (***red***) or 5-*d*-**3** (***blue***). The ***red points*** are the quantities of Y• determined in the freeze-quench EPR experiment with **3**. The ***green points*** are the quantities of the ferryl species determined in the freeze-quench Mössbauer experiment with **3**. The ***green***, ***black and gray traces***, which correspond to the right-hand y-axis, are concentrations of state **b** in the reaction with **3** (***green***), **c** in the reaction with **3** (***black***), and **c** in the reaction with 5-*d*-**3** (***gray***) predicted by simulations based on the kinetic mechanism given below the plot, which corresponds to the chemical mechanism in *Fig. 2C* but takes into account the unproductive pathway (k = 0.32 s^{-1}) for decay of the ferryl species (**b**) revealed by the 5-*d*-**3** $A_{410\ dropline}$ trace and the fact that only 0.34 of the total enzyme reacts.

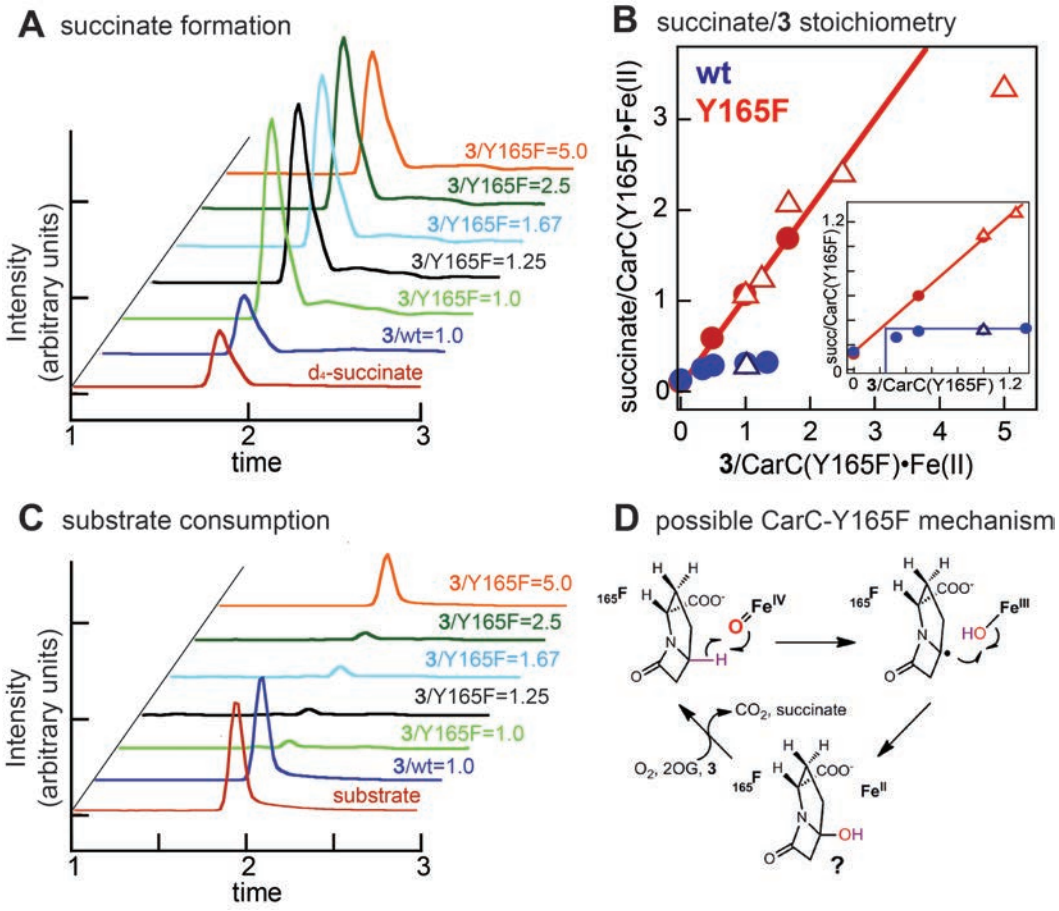

Figure S8. LC-MS analysis of the CarC and CarC-Y165F reaction stoichiometries and the hypothetical altered mechanism of the variant protein that could rationalize the data. (***A***) Single-ion chromatograms showing succinate (*m*/*z* = 117) produced with varying **3**/CarC ratio with the wild-type and Y165F variant proteins. The ***red trace*** at front is the chromatogram for *m*/*z* = 121 corresponding to the d_4-succinate internal standard. (***B***) Equivalents succinate produced as a function of **3**/CarC ratio for the wild-type (***blue***) and Y165F (***red***) proteins. The inset is a blowup of the region of **3**/CarC ≤ ~ 1. The slope of the plot for the Y165F variant gives the succinate/**3** reaction stoichiometry (1.0) and shows a linear dependence, implying full conversion, for **3**/CarC-Y165F < ~ 3. This result shows that the variant protein can perform at least 3 turnovers. By contrast, the plateau of the plot at succinate/CarC•Fe(II) ~ 0.33 implies both that the reaction of the wild-type protein is stoichiometric under these conditions and that only one-third of the Fe(II) sites react. (***C***) Chromatograms reporting the quantity of substrate remaining under the same conditions as in ***A***. The red trace in front is a control chromatogram obtained by injecting just the substrate. All reactions had 1.0 mM 2OG, 0.25 mM **3** [except the reaction having **3**/CarC•Fe(II) = 0], and ambient O_2 along with 0.075 mM d_4-succinate as internal MS standard for quantification of succinate produced in the reaction. An aliquot of an O_2-free CarC(-Y165F) solution containing 0.8 equiv Fe(II) was added to the aerobic solution of 2OG, **3** and d_4-succinate to give the indicated ratio of **3**/CarC•Fe(II), and the reaction was allowed to proceed to completion. The protein was removed by using a Nanosep centrifugal filter, and 5 μL of the filtrate was analyzed by LC-MS as in the

experiment of *Fig. 4D*. Note that, in this experiment, reactions were not terminated by treatment with formic acid, permitting the unconsumed substrate **3** and product **4** generated by the wild-type enzyme to survive for LC-MS detection, where they are not resolved in the chromatography. Consequently, stereoinversion is not detected by this analysis (***C, compare red and blue traces***), and the obvious consumption of **3** by the Y165F variant seen in ***C*** reflects conversion to a product different from **4**. (***D***) The hypothetical hydroxylation of C5 resulting from the Y165F substitution that could rationalize the catalytic consumption of **3** by the variant protein via an outcome other than stereoinversion.

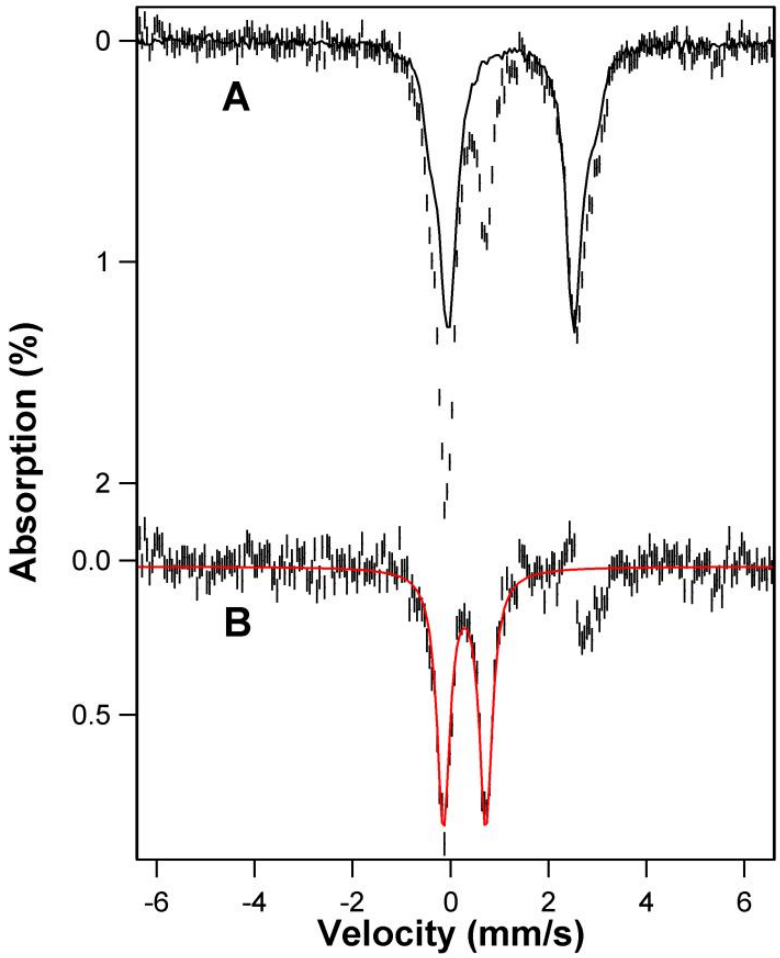

Figure S9. Mössbauer spectroscopic evidence for accumulation of a ferryl precursor to the Y• (*Fig. 2C, state* ***b***) in the reaction of the CarC•Fe(II)•2OG•**3** complex with O_2. (***A***) 4.2-K/53-mT Mössbauer spectrum (***vertical bars***) of the 0.15-s sample prepared as described in Materials and Methods. The ***solid black trace*** in ***A*** is the spectrum of the reactant complex plotted at 55% of the intensity of the 0.15-s spectrum. (***B***) The difference spectrum generated by subtraction of the two spectra in ***A***. The ***red trace*** is the simulated spectrum of the presumptive ferryl species (parameters δ = 0.28 mm/s, ΔE_Q = 0.87 mm/s, linewidth = 0.30 mm/s) plotted at 24% of the intensity in ***A***.

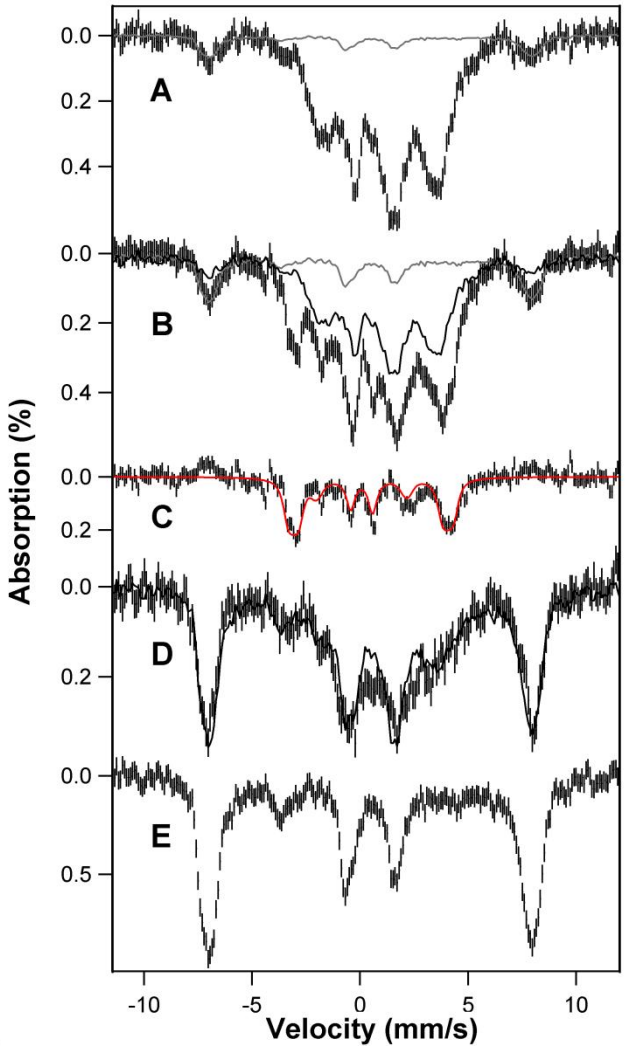

Figure S10. Low-temperature (4.2-K) high-field (8.0-T) Mössbauer spectra characterizing the Fe(IV) (ferryl) intermediate and the Fe(III) species in the CarC reaction. (***A***) Spectrum of the reactant complex (***vertical bars***), revealing a contaminant of oxidized product (***gray trace***, which is the experimental spectrum from the 10-min sample, ***E***, plotted at 10% of the intensity of ***A***). (***B***) Spectrum of the 0.15-s sample from *fig. S9* (***bars***), showing a 20% contribution from the spectrum of the 10-min sample (***gray trace***) and 55% contribution from the spectrum of the reactant complex (***black trace***). (**C**) Difference spectrum, revealing the hallmark features of the high-spin Fe(IV) intermediate, after subtracting these other contributions from the experimental spectrum in ***B***. The red trace is a theoretical simulation of the spectrum assuming an $S = 2$ electron-spin ground state and the following parameters: $D = 10$ cm^{-1}, $E/D = 0$, $\delta = 0.28$ mm/s, $\Delta E_Q = -0.87$ mm/s, $\eta = 0$, $A_x/g_n\beta_n = -18.5$ T, $A_y/g_n\beta_n = -15.8$ T, $A_z/g_n\beta_n = -30$ T, and linewidth = 0.33 mm/s. The breadth of the outer lines in the derived spectrum suggests slight (~15%) anisotropy of the internal field in the *xy*-plane, which could arise from anisotropy in $A_x/g_n\beta_n$ and $A_y/g_n\beta_n$ (as simulated here), a small, non-zero value of the rhombicity (E/D), or both. (***D***) The experimental spectrum of the 3-s freeze-quenched sample (***bars***), plotted with a summed contribution of 55% of the spectrum of the 10-min sample and 35% of spectrum A (***black trace***). (***E***) Experimental spectrum of the 10-min sample.

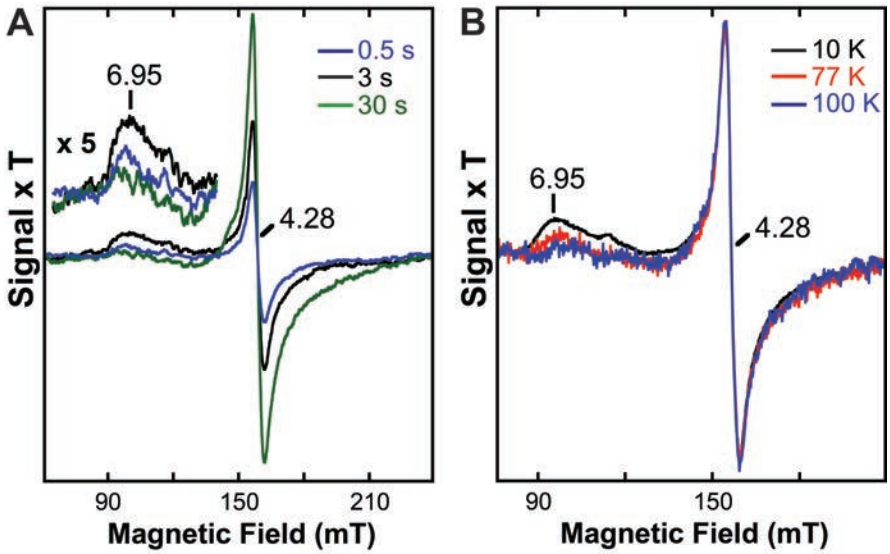

Figure S11. (***A***) X-band EPR spectra at 10 K in the low-field (high-*g*-value) region for the freeze-quenched samples in *Fig. 4C*. (***B***) X-band EPR spectra in the low-field region for the 3-s freeze-quenched sample from *Fig. 4C* acquired at 10 K (***black trace***), 77 K (***red trace***), and 100 K (***blue trace***). The breadth of the low-field resonances most likely results from structural heterogeneity of the Fe(III) species. Spectral simulations show that the dipolar coupling with the Y• at the expected distance of ~ 7 Å should not result in broadening of this sort.

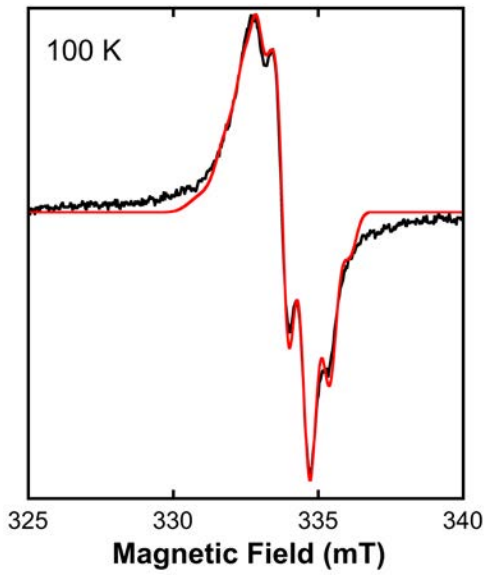

Figure S12. X-band EPR spectrum at 100 K (***black trace***) of the 3-s freeze-quenched sample from *Fig. 4C* showing the recognizable ^{1}H hyperfine interactions characteristic of a Y•. The ***red trace*** is a theoretical simulation with parameters **g** = (2.014, 2.007, 2.003), $A_{H\beta 1,2}$ = (29, 23, 23) MHz, $A_{H3,5}$ = (28, 8, 18) MHz. Although ^{1}H-hyperfine coupling consistent with a Y• is evident, the 100-K spectrum still exhibits manifestations of the

magnetic coupling to the Fe(III) center that is responsible for obscuring the characteristic ^{1}H-hyperfine coupling in the 10-K spectrum. First, the anisotropy in **g** is unusually large and the principal values somewhat high. However, the parameters of the spin-Hamiltonian are correlated and cannot be uniquely assigned from the analysis of this single spectrum. Collection of additional spectra under different experimental conditions (in progress) would be required for the unambiguous determination of these parameters and may reveal more usual principal values of **g**. Second, as apparent from the imperfect agreement between the simulation and data, the experimental spectrum still has intensity in the "wings" outside the envelope of the typical Y• spectrum. The observation of a weak g = 6.95 signal at 100 K indicates that the Fe(III) center is still not fully in the fast-relaxing regime at this higher temperature and explains the residual coupling to the Y•.

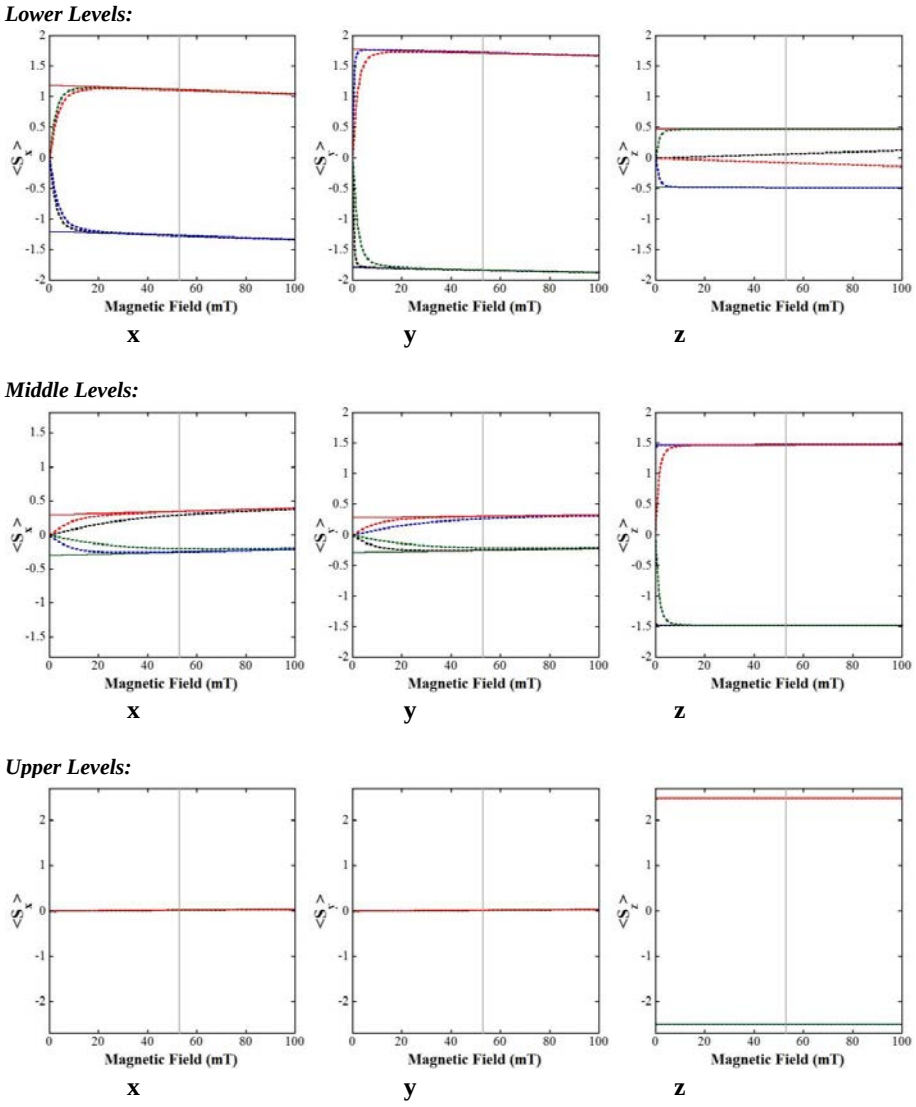

Figure S13. Dependence of the spin-expectation values of a mononuclear high-spin Fe(III) center (<S_{Fe}>) on the externally applied magnetic field. Solid lines are calculated

with the following parameters: S_{Fe} = 5/2, D_{Fe} = 1.5 cm^{-1}, $(E/D)_{Fe}$ = 0.05, and g_{Fe} (2.0, 2.0, 2.0). The external magnetic field is oriented along the molecular x-direction (left column), y-direction (middle column), or z-direction (right column). $\langle S_{Fe} \rangle$ associated with the two states of the ground Kramers doublet are depicted in the top row, while those associated with the first and second excited Kramers doublet are depicted in the middle row and bottom row, respectively. The dotted lines are calculated for a high-spin Fe(III) site with the above parameters and assuming a magnetic point dipole interaction with a S = 1/2 spin at a distance of 7 Å. Note that the dipolarly coupled system contains twice as many (12) states compared to the uncoupled Fe(III) system. Vertical gray lines indicate the value of the externally applied magnetic field employed in the low-field Mössbauer spectra (53 mT). Comparison of the solid and dotted lines reveals that $\langle S_{Fe} \rangle$ of the dipolarly coupled system is >95% of the values of the uncoupled Fe(III) system. Thus, the magnetic dipole interaction is not expected to perturb the 53-mT Mössbauer spectra. Calculations were carried out with the program Spinham developed by Prof. Michael Hendrich (Carnegie Mellon University).

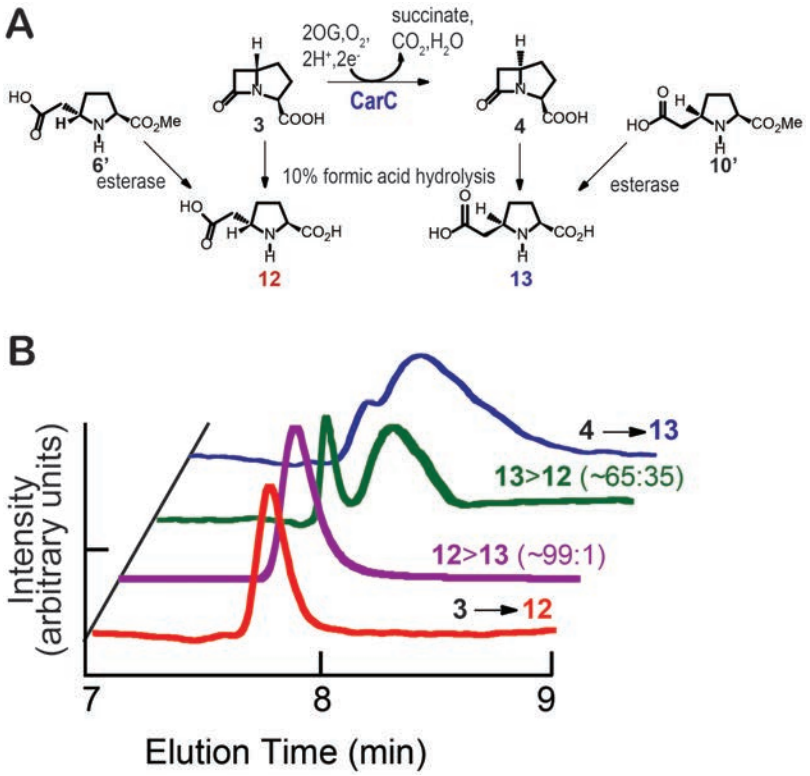

Figure S14. Tools in the LC-MS analysis of the CarC reaction. (***A***) Chemical and enzymatic reactions important in the analysis. (***B***) Chromatograms of acid-hydrolyzed samples of the synthetic substrate **3** (***red***) and product **4** (***blue***) and the synthetic standards for their hydrolysis products, **12** (***purple***) and **13** (***green***), respectively. Details of the LC-MS method and the methods of preparation and composition of the synthetic standards are provided above in **Materials and Methods**.

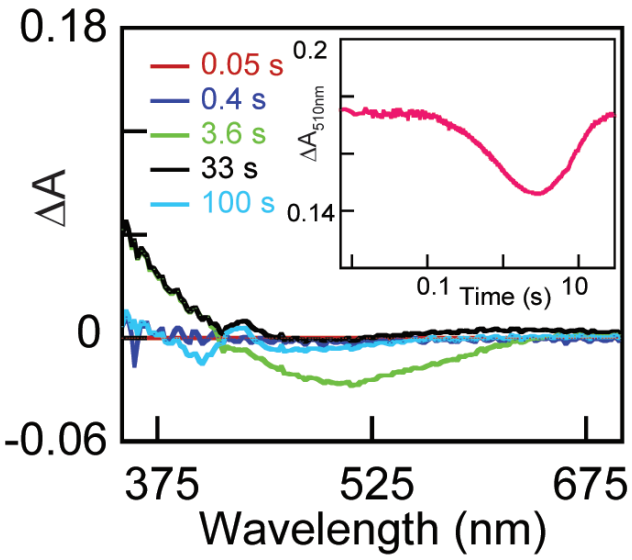

Figure S15. Stopped-flow absorption data suggesting that only a fraction of the Fe(II) centers react also in the CarC-Y165F variant. The reaction was carried out by mixing O_2-saturated buffer at 5 °C with an equal volume of an O_2-free solution containing 1.0 mM CarC-Y165F, 0.80 mM Fe(II), 20 mM 2OG, and 10 mM **3**. The ***main figure*** shows difference spectra at the indicated reaction times obtained by subtracting the first reliable spectrum (5 ms) from the spectra at these later times. The ***inset*** shows the change in absorbance at 510 nm arising from the Fe(II) → 2OG charge-transfer transition. This transition typically has an associated molar absorption coefficient of ~ 180 $M^{-1}cm^{-1}$. The amplitude of decay of A_{510} (~ 0.026) would thus correspond to ~ 0.37 equiv of the complex.

Table S1. Data collection and refinement statistics for the X-ray crystal structure of the *P. carotovorum* CarC•Fe(II)•2OG•**3** complex.

	CarC•Fe(II)•2OG•**3**
Data collection	
Wavelength	0.97857 Å
Space group	$C222_1$
Cell dimensions	
a, *b*, *c* (Å)	80.251, 165.778, 146.581
Resolution (Å)	30.00-2.10 (2.14-2.10)
R_{merge}	0.089 (0.873)
$\langle I / s \rangle$	28.2 (2.2)
Completeness (%)	100.0 (100.0)
Redundancy	7.5 (7.1)
Refinement	
Resolution (Å)	30.00-2.10
No. reflections	54307
R_{work} / R_{free}	0.1983/0.2357
No. atoms	
Protein	6519
Ion/ligand	61
Water	411
B-factors	
Protein	37.8
Ion/ligand	51.3
Water	47.4
r.m.s. deviations	
Bond lengths (Å)	0.005
Bond angles (°)	0.980

References and Notes

1. R. P. Elander, Industrial production of beta-lactam antibiotics. *Appl. Microbiol. Biotechnol.* **61**, 385–392 (2003). Medline doi:10.1007/s00253-003-1274-y

2. R. B. Hamed, J. R. Gomez-Castellanos, L. Henry, C. Ducho, M. A. McDonough, C. J. Schofield, The enzymes of β-lactam biosynthesis. *Nat. Prod. Rep.* **30**, 21–107 (2013). Medline doi:10.1039/c2np20065a

3. S. J. Coulthurst, A. M. Barnard, G. P. Salmond, Regulation and biosynthesis of carbapenem antibiotics in bacteria. *Nat. Rev. Microbiol.* **3**, 295–306 (2005). Medline doi:10.1038/nrmicro1128

4. J. S. Bradley, J. Garau, H. Lode, K. V. Rolston, S. E. Wilson, J. P. Quinn, Carbapenems in clinical practice: A guide to their use in serious infection. *Int. J. Antimicrob. Agents* **11**, 93–100 (1999). Medline doi:10.1016/S0924-8579(98)00094-6

5. The antibiotic alarm. *Nature* **495**, 141 (2013). Medline doi:10.1038/495141a

6. J. S. Kahan, F. M. Kahan, R. Goegelman, S. A. Currie, M. Jackson, E. O. Stapley, T. W. Miller, A. K. Miller, D. Hendlin, S. Mochales, S. Hernandez, H. B. Woodruff, J. Birnbaum, Thienamycin, a new beta-lactam antibiotic. I. Discovery, taxonomy, isolation and physical properties. *J. Antibiot. (Tokyo)* **32**, 1–12 (1979). Medline doi:10.7164/antibiotics.32.1

7. W. L. Parker, M. L. Rathnum, J. S. Wells Jr., W. H. Trejo, P. A. Principe, R. B. Sykes, SQ 27,860, a simple carbapenem produced by species of *Serratia* and *Erwinia*. *J. Antibiot. (Tokyo)* **35**, 653–660 (1982). Medline doi:10.7164/antibiotics.35.653

8. S. J. McGowan, M. Sebaihia, L. E. Porter, G. S. Stewart, P. Williams, B. W. Bycroft, G. P. Salmond, Analysis of bacterial carbapenem antibiotic production genes reveals a novel beta-lactam biosynthesis pathway. *Mol. Microbiol.* **22**, 415–426 (1996). Medline doi:10.1046/j.1365-2958.1996.00125.x

9. A. L. Demain, R. P. Elander, The beta-lactam antibiotics: Past, present, and future. *Antonie van Leeuwenhoek* **75**, 5–19 (1999). Medline doi:10.1023/A:1001738823146

10. R. F. Li, A. Stapon, J. T. Blanchfield, C. A. Townsend, Three unusual reactions mediate carbapenem and carbapenam biosynthesis. *J. Am. Chem. Soc.* **122**, 9296–9297 (2000). doi:10.1021/ja001723l

11. B. Gerratana, S. O. Arnett, A. Stapon, C. A. Townsend, Carboxymethylproline synthase from *Pectobacterium carotorova*: A multifaceted member of the crotonase superfamily. *Biochemistry* **43**, 15936–15945 (2004). Medline doi:10.1021/bi0483662

12. R. B. Hamed, J. Mecinović, C. Ducho, T. D. Claridge, C. J. Schofield, Carboxymethylproline synthase catalysed syntheses of functionalised *N*-heterocycles. *Chem. Commun.* **46**, 1413–1415 (2010). Medline doi:10.1039/b924519g

13. B. Gerratana, A. Stapon, C. A. Townsend, Inhibition and alternate substrate studies on the mechanism of carbapenam synthetase from *Erwinia carotovora*. *Biochemistry* **42**, 7836–7847 (2003). Medline doi:10.1021/bi034361d

14. A. Stapon, R. Li, C. A. Townsend, Carbapenem biosynthesis: Confirmation of stereochemical assignments and the role of CarC in the ring stereoinversion process from *L*-proline. *J. Am. Chem. Soc.* **125**, 8486–8493 (2003). Medline doi:10.1021/ja034248a

15. R. B. Woodward, Penems and related substances. *Philos. Trans. R. Soc. Lond. B Biol. Sci.* **289**, 239–250 (1980). Medline doi:10.1098/rstb.1980.0042

16. A. Nangia, K. Biradha, G. R. Desiraju, Correlation of biological activity in beta-lactam antibiotics with Woodward and Cohen structural parameters - A Cambridge database study. *J. Chem. Soc. Perk. Trans.* **2**, 943 (1996). doi:10.1039/p29960000943

17. R. B. Hamed, E. T. Batchelar, J. Mecinović, T. D. Claridge, C. J. Schofield, Evidence that thienamycin biosynthesis proceeds via C-5 epimerization: ThnE catalyzes the formation of (2*S*,5*S*)-*trans*-carboxymethylproline. *ChemBioChem* **10**, 246–250 (2009). Medline doi:10.1002/cbic.200800652

18. R. B. Hamed, J. R. Gomez-Castellanos, A. Thalhammer, D. Harding, C. Ducho, T. D. Claridge, C. J. Schofield, Stereoselective C-C bond formation catalysed by engineered carboxymethylproline synthases. *Nat. Chem.* **3**, 365–371 (2011). Medline doi:10.1038/nchem.1011

19. R. B. Hamed, L. Henry, J. R. Gomez-Castellanos, J. Mecinović, C. Ducho, J. L. Sorensen, T. D. Claridge, C. J. Schofield, Crotonase catalysis enables flexible production of functionalized prolines and carbapenams. *J. Am. Chem. Soc.* **134**, 471–479 (2012). Medline doi:10.1021/ja208318d

20. M. J. Bodner, R. M. Phelan, M. F. Freeman, R. Li, C. A. Townsend, Non-heme iron oxygenases generate natural structural diversity in carbapenem antibiotics. *J. Am. Chem. Soc.* **132**, 12–13 (2010). Medline doi:10.1021/ja907320n

21. R. P. Hausinger, FeII/α-ketoglutarate-dependent hydroxylases and related enzymes. *Crit. Rev. Biochem. Mol. Biol.* **39**, 21–68 (2004). Medline doi:10.1080/10409230490440541

22. C. Krebs, D. Galonić Fujimori, C. T. Walsh, J. M. Bollinger Jr., Non-heme Fe(IV)-oxo intermediates. *Acc. Chem. Res.* **40**, 484–492 (2007). Medline doi:10.1021/ar700066p

23. E. I. Solomon, T. C. Brunold, M. I. Davis, J. N. Kemsley, S. K. Lee, N. Lehnert, F. Neese, A. J. Skulan, Y. S. Yang, J. Zhou, Geometric and electronic structure/function correlations in non-heme iron enzymes. *Chem. Rev.* **100**, 235–350 (2000). Medline doi:10.1021/cr9900275

24. M. Costas, M. P. Mehn, M. P. Jensen, L. Que Jr., Dioxygen activation at mononuclear nonheme iron active sites: enzymes, models, and intermediates. *Chem. Rev.* **104**, 939–986 (2004). Medline doi:10.1021/cr020628n

25. M. Topf, G. M. Sandala, D. M. Smith, C. J. Schofield, C. J. Easton, L. Radom, The unusual bifunctional catalysis of epimerization and desaturation by carbapenem synthase. *J. Am. Chem. Soc.* **126**, 9932–9933 (2004). Medline doi:10.1021/ja047899v

26. T. Borowski, E. Broclawik, C. J. Schofield, P. E. M. Siegbahn, Epimerization and desaturation by carbapenem synthase (CarC). A hybrid DFT study. *J. Comput. Chem.* **27**, 740–748 (2006). Medline doi:10.1002/jcc.20384

27. R. M. Phelan, B. J. DiPardo, C. A. Townsend, A high-throughput screen for the engineered production of β-lactam antibiotics. *ACS Chem. Biol.* **7**, 835–840 (2012). Medline doi:10.1021/cb200504g

28. R. M. Phelan, C. A. Townsend, Mechanistic insights into the bifunctional non-heme iron oxygenase carbapenem synthase by active site saturation mutagenesis. *J. Am. Chem. Soc.* **135**, 7496–7502 (2013). Medline doi:10.1021/ja311078s

29. J. Zhou, W. L. Kelly, B. O. Bachmann, M. Gunsior, C. A. Townsend, E. I. Solomon, Spectroscopic studies of substrate interactions with clavaminate synthase 2, a multifunctional α-KG-dependent non-heme iron enzyme: Correlation with mechanisms and reactivities. *J. Am. Chem. Soc.* **123**, 7388–7398 (2001). Medline doi:10.1021/ja004025+

30. J. M. Bollinger Jr., C. Krebs, Stalking intermediates in oxygen activation by iron enzymes: Motivation and method. *J. Inorg. Biochem.* **100**, 586–605 (2006). Medline doi:10.1016/j.jinorgbio.2006.01.022

31. J. M. Bollinger Jr., W. H. Tong, N. Ravi, B. H. Huynh, D. E. Edmondson, J. A. Stubbe, Use of rapid kinetics methods to study the assembly of the diferric-tyrosyl radical cofactor of *E. coli* ribonucleotide reductase. *Methods Enzymol.* **258**, 278–303 (1995). Medline doi:10.1016/0076-6879(95)58052-2

32. H. R. Pfaendler, J. Gosteli, R. B. Woodward, G. Rihs, Structure, reactivity, and biological activity of strained bicyclic beta-lactams. *J. Am. Chem. Soc.* **103**, 4526–4531 (1981). doi:10.1021/ja00405a039

33. M. C. Sleeman, P. Smith, B. Kellam, S. R. Chhabra, B. W. Bycroft, C. J. Schofield, Biosynthesis of carbapenem antibiotics: New carbapenam substrates for carbapenem synthase (CarC). *ChemBioChem* **5**, 879–882 (2004). Medline doi:10.1002/cbic.200300908

34. B. W. Bycroft, S. R. Chhabra, A chiral synthesis of *trans*-carbapenam-3-carboxylic acid and the assignment of (3*S*,5*S*) configuration to the corresponding product from *Serratia* and *Erwinia* species. *J. Chem. Soc. Chem. Commun.*, 423 (1989). doi:10.1039/c39890000423

35. A. Avenoza, J. I. Barriobero, J. H. Busto, J. M. Peregrina, Enantiopure synthesis of all four stereoisomers of carbapenam-3-carboxylic acid methyl ester. *J. Org. Chem.* **68**, 2889–2894 (2003). Medline doi:10.1021/jo026804+

36. I. J. Clifton, L. X. Doan, M. C. Sleeman, M. Topf, H. Suzuki, R. C. Wilmouth, C. J. Schofield, Crystal structure of carbapenem synthase (CarC). *J. Biol. Chem.* **278**, 20843–20850 (2003). Medline doi:10.1074/jbc.M213054200

37. L. M. Hoffart, E. W. Barr, R. B. Guyer, J. M. Bollinger Jr., C. Krebs, Direct spectroscopic detection of a C-H-cleaving high-spin Fe(IV) complex in a prolyl-4-hydroxylase. *Proc. Natl. Acad. Sci. U.S.A.* **103**, 14738–14743 (2006). Medline doi:10.1073/pnas.0604005103

38. D. P. Galonić, E. W. Barr, C. T. Walsh, J. M. Bollinger Jr., C. Krebs, Two interconverting Fe(IV) intermediates in aliphatic chlorination by the halogenase CytC3. *Nat. Chem. Biol.* **3**, 113–116 (2007). Medline doi:10.1038/nchembio856

39. M. L. Matthews, C. M. Krest, E. W. Barr, F. H. Vaillancourt, C. T. Walsh, M. T. Green, C. Krebs, J. M. Bollinger, Substrate-triggered formation and remarkable stability of the C-H bond-cleaving chloroferryl intermediate in the aliphatic halogenase, SyrB2. *Biochemistry* **48**, 4331–4343 (2009). Medline doi:10.1021/bi900109z

40. M. L. Matthews, C. S. Neumann, L. A. Miles, T. L. Grove, S. J. Booker, C. Krebs, C. T. Walsh, J. M. Bollinger Jr., Substrate positioning controls the partition between halogenation and hydroxylation in the aliphatic halogenase, SyrB2. *Proc. Natl. Acad. Sci. U.S.A.* **106**, 17723–17728 (2009). Medline doi:10.1073/pnas.0909649106

41. J. C. Price, E. W. Barr, B. Tirupati, J. M. Bollinger Jr., C. Krebs, The first direct characterization of a high-valent iron intermediate in the reaction of an α-ketoglutarate-dependent dioxygenase: A high-spin FeIV complex in taurine/α-ketoglutarate dioxygenase (TauD) from *Escherichia coli*. *Biochemistry* **42**, 7497–7508 (2003). Medline doi:10.1021/bi030011f

42. J. M. Bollinger Jr., J. C. Price, L. M. Hoffart, E. W. Barr, C. Krebs, Mechanism of taurine: α-Ketoglutarate dioxygenase (TauD) from *Escherichia coli*. *Eur. J. Inorg. Chem.* **2005**, 4245–4254 (2005). doi:10.1002/ejic.200500476

43. K. P. McCusker, J. P. Klinman, Modular behavior of tauD provides insight into the origin of specificity in α-ketoglutarate-dependent nonheme iron oxygenases. *Proc. Natl. Acad. Sci. U.S.A.* **106**, 19791–19795 (2009). Medline doi:10.1073/pnas.0910660106

44. J. T. Groves, Key elements of the chemistry of cytochrome-P-450: The oxygen rebound mechanism. *J. Chem. Educ.* **62**, 928 (1985). doi:10.1021/ed062p928

45. C. Pedregal, J. Ezquerra, A. Escribano, M. C. Carreño, J. L. G. Ruano, Highly chemoselective reduction of *N*-Boc protected lactams. *Tetrahedron Lett.* **35**, 2053–2056 (1994). doi:10.1016/S0040-4039(00)73047-4

46. I. Collado, J. Ezquerra, J. J. Vaquero, C. Pedregal, Diastereoselective functionalization of 5-hydroxy prolinates by tandem Horner-Emmons-Michael reaction. *Tetrahedron Lett.* **35**, 8037–8040 (1994). doi:10.1016/0040-4039(94)80043-X

47. S. Ranatunga, W. Liyanage, J. R. Del Valle, Synthesis and conformational analysis of bicyclic extended dipeptide surrogates. *J. Org. Chem.* **75**, 5113–5125 (2010). Medline doi:10.1021/jo1008433

48. B. W. Bycroft, S. R. Chhabra, B. Kellam, P. Smith, Convenient syntheses of (3*S*,5*S*)-carbapenam-3-carboxylates and their biosynthetic relevance. *Tetrahedron Lett.* **44**, 973–976 (2003). doi:10.1016/S0040-4039(02)02731-4

49. J. M. Bollinger Jr., W. H. Tong, N. Ravi, B. H. Huynh, D. E. Edmonson, J. A. Stubbe, Mechanism of assembly of the tyrosyl radical-diiron(III) cofactor of *Escherichia coli* ribonucleotide reductase. 2. kinetics of the excess Fe^{2+} reaction by optical, EPR, and Mössbauer spectroscopies. *J. Am. Chem. Soc.* **116**, 8015–8023 (1994). doi:10.1021/ja00097a008

50. Z. Otwinowski, W. Minor, Processing of X-ray diffraction data collected in oscillation mode. *Methods Enzymol.* **276**, 307–326 (1997). doi:10.1016/S0076-6879(97)76066-X

51. A. J. McCoy, R. W. Grosse-Kunstleve, L. C. Storoni, R. J. Read, Likelihood-enhanced fast translation functions. *Acta Crystallogr. D Biol. Crystallogr.* **61**, 458–464 (2005). Medline doi:10.1107/S0907444905001617

52. G. N. Murshudov, A. A. Vagin, E. J. Dodson, Refinement of macromolecular structures by the maximum-likelihood method. *Acta Crystallogr. D Biol. Crystallogr.* **53**, 240–255 (1997). Medline doi:10.1107/S0907444996012255

53. P. Emsley, K. Cowtan, Coot: Model-building tools for molecular graphics. *Acta Crystallogr. D Biol. Crystallogr.* **60**, 2126–2132 (2004). Medline doi:10.1107/S0907444904019158

54. A. W. Schüttelkopf, D. M. F. van Aalten, PRODRG: A tool for high-throughput crystallography of protein-ligand complexes. *Acta Crystallogr. D Biol. Crystallogr.* **60**, 1355–1363 (2004). Medline doi:10.1107/S0907444904011679

55. E. Krissinel, K. Henrick, Secondary-structure matching (SSM), a new tool for fast protein structure alignment in three dimensions. *Acta Crystallogr. D Biol. Crystallogr.* **60**, 2256–2268 (2004). Medline doi:10.1107/S0907444904026460

56. R. A. Laskowski, M. W. MacArthur, D. S. Moss, J. M. Thornton, *PROCHECK*: A program to check the stereochemical quality of protein structures. *J. Appl. Cryst.* **26**, 283–291 (1993). doi:10.1107/S0021889892009944

57. V. B. Chen, W. B. Arendall 3rd, J. J. Headd, D. A. Keedy, R. M. Immormino, G. J. Kapral, L. W. Murray, J. S. Richardson, D. C. Richardson, MolProbity: All-atom structure validation for macromolecular crystallography. *Acta Crystallogr. D Biol. Crystallogr.* **66**, 12–21 (2010). Medline doi:10.1107/S0907444909042073

58. L. F. Ten Eyck, Fast Fourier transform calculation of electron density maps. *Methods Enzymol.* **115**, 324–337 (1985). Medline doi:10.1016/0076-6879(85)15024-X